CRYSTAL GROWTH & DESIGN

pubs.acs.org/crystal

Communication

Solid-State Structure of Xanthine Determined by a Combination of 3D Electron Diffraction, Powder X-ray Diffraction, and DFT-D Calculations

Colan E. Hughes, Benson M. Kariuki, Abrar Almetahr, Jessica Saint-Mart, Andrew Williams, Laura Samperisi, and Kenneth D. M. Harris*

Cite This: https://doi.org/10.1021/acs.cgd.4c01717

Read Online

ACCESS | Metrics & More | Article Recommendations | Supporting Information

ABSTRACT: In the crystalline state, xanthine plays a significant role in several biological systems. For example, pathological crystallization of xanthine causes renal stones in humans and bladder stones in cats and dogs, while xanthine crystals can also serve as functional optical materials, including their role as reflective mirrors in the eye-like organs of certain insects. To understand the role of crystalline xanthine in such biological processes and functions, knowledge of the crystal structure is essential. However, crystal structure determination has so far proved elusive, as xanthine is recalcitrant to the formation of crystals suitable for single-crystal XRD, and severe preferred orientation in powder samples of xanthine has prevented structure determination from powder XRD data. Here we report the crystal structure of xanthine based on the analysis of 3D electron diffraction (3D-ED) data recorded for microcrystals in a powder sample, in conjunction with periodic DFT-D calculations and the analysis of powder XRD data. In common with certain other purines, the crystal structure of xanthine is a layered structure containing planar hydrogen-bonded sheets in which all hydrogen-bond donor and acceptor groups are engaged in intermolecular hydrogen bonds. Considering the tautomeric form of xanthine in the crystal structure, analysis of the 3D-ED data supports the presence of the N7H tautomer (the tautomer of lowest energy for an isolated xanthine molecule). However, the corresponding crystal structure containing the N9H tautomer is essentially isostructural, as it differs from the structure containing the N7H tautomer only in the position of the H atom within each intermolecular N−H···N hydrogen bond in the structure. Interestingly, the difference in energy (per molecule of xanthine) between the crystal structures containing the N7H and N9H tautomers is significantly lower than the difference in energy of an isolated xanthine molecule in the N7H and N9H tautomers.

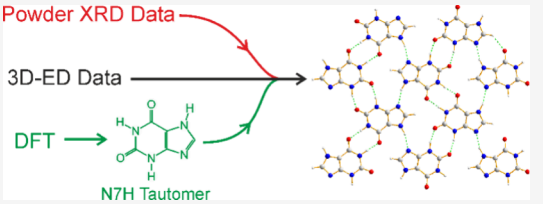

The purine base xanthine (Figure 1) is an important metabolite in a wide variety of living systems and is produced by the purine degradation pathway from guanine or hypoxanthine. In the crystalline state, xanthine is implicated in important biological phenomena. In healthy individuals, the enzyme xanthine oxidase degrades xanthine to uric acid. However, a genetic disorder called xanthine urolithiasis[1,2] causes a deficiency of xanthine oxidase, resulting in increased levels of xanthine in the blood that can lead to accumulation of xanthine crystals in human kidneys (renal stones) or xanthine bladder stones in cats[3,4] and dogs.[5] Xanthine urolithiasis commonly leads to urinary tract infections and, more rarely, to acute renal failure,[6] joint disease, and other serious conditions.[7] A completely different biological role of crystalline xanthine arises in some species of insects that use xanthine as a functional optical material. Highly reflective, plate-like crystals of xanthine form a mirror that is used to enhance photon capture in eye-like organs (ocelli) in jumping bristletails[8−10] and has stimulated interest in the potential to use xanthine crystals as the basis for bioinspired optical materials.[11,12] Recently, it has also been recognized[13] that xanthine (and

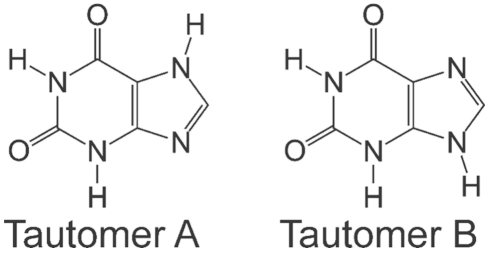

Figure 1. Molecular structure of xanthine in the two tautomeric forms of lowest energy, which differ in the position of one H atom. Tautomers A and B are often designated as the N7H and N9H tautomers, respectively.

Received: December 19, 2024
Revised: January 24, 2025
Accepted: January 24, 2025

other purines such as hypoxanthine) can exist as a dopant in biogenic crystals of guanine and may play an important role in controlling crystal morphology.[14]

Given the growing realization of the importance of crystalline xanthine in biological systems, knowledge of the crystal structure of xanthine is clearly important, for example to facilitate the design of effective strategies to inhibit pathological crystallization and to rationalize the role of crystalline xanthine in biological optical systems. However, crystal structure determination of xanthine has proven elusive, and xanthine is one of the few purines for which a crystal structure of the pure material has not yet been reported in the CSD. Examples of structures in the CSD that contain xanthine include the dihydrate of a perchlorate salt,[15] the tetrahydrate of a sodium salt,[16] and various structures containing xanthine as a ligand in metal complexes.

Crystal structure determination of xanthine is challenging for several reasons, including (i) the fact that xanthine has very low solubility in common solvents,[17−19] which limits the prospects to prepare crystals of suitable size and quality for single-crystal XRD by standard crystallization methods, and (ii) the fact that powder samples of xanthine exhibit severe preferred orientation, which causes significant challenges in structure determination from powder XRD data. As experimental powder XRD data for xanthine are typically dominated by a single peak, with relatively few other peaks of significant intensity, even the task of determining a reliable unit cell from powder XRD data is challenging.[20]

Given these challenges, an alternative approach is to tackle structure determination from 3D electron diffraction (3D-ED) data recorded for microcrystals in a powder sample. Progress in the development of 3D-ED techniques[21−32] has created significant new opportunities to determine the structures of microcrystalline materials, such as xanthine, that have eluded structure determination from single-crystal XRD or powder XRD, as demonstrated widely in recent years.[33−38]

In this paper, we report the crystal structure of xanthine determined from 3D-ED data, with the structure determination process augmented by periodic DFT-D calculations and the analysis of powder XRD data.

RESULTS AND DISCUSSION

Crystallization of Xanthine. All studies reported here were carried out on a synthetic sample of xanthine obtained commercially, which was shown by powder XRD (Figure 2a,b) to be a crystalline phase. Solubility tests in some common solvents showed that xanthine is slightly soluble in ethanol and essentially insoluble in water and methanol. Crystallization of xanthine by slow evaporation of solvent from a saturated solution of xanthine in ethanol (see Section S1; Supporting Information) produced a very fine powder that was shown by powder XRD (Figure 2c) to be the same crystalline phase as the commercial sample of xanthine. However, given the low solubility in ethanol, saturated solutions contain only a small amount of solute and therefore only small amounts of crystallized product can be obtained in crystallization experiments. For this reason, most of the studies reported here were carried out using the commercial crystalline sample rather than materials prepared by crystallization from ethanol, recalling that both of these materials represent the same phase of xanthine.

Crystal Structure Determination. As shown in Figure 2, experimental powder XRD data for xanthine are dominated by a strong peak at $2\theta \approx 28°$ (Cu Kα_1 radiation), and all other peaks have significantly lower intensities. Extensive attempts to apply standard indexing methods to determine a reliable unit cell from powder XRD data proved unsuccessful, and our structure determination strategy focused instead on the analysis of 3D-ED data. The 3D-ED data were recorded for microcrystals of xanthine (typical microcrystals, with maximum dimension ca. 0.6 μm, are shown in Figure S1) at ambient temperature (293 K) on an ELDICO ED-1 electron diffractometer (acceleration voltage = 160 kV; λ = 0.02851 Å) under continuous rotation with a tilt range from −60° to +60°. No significant beam damage was detected during the measurements. In total, 15 data sets were recorded from 15 individual microcrystals with a diffraction resolution of ca. 1.0 Å.

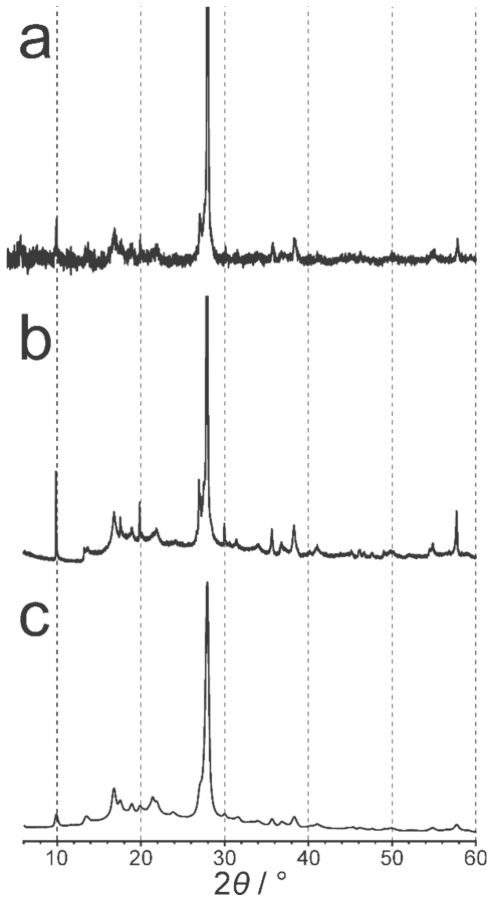

Figure 2. Powder XRD data recorded for samples of xanthine: (a) commercial sample (laboratory powder XRD data; Cu Kα_1), (b) commercial sample (synchrotron powder XRD data adjusted to a wavelength corresponding to Cu Kα_1), and (c) sample crystallized from ethanol (single-crystal XRD instrument; Cu Kα). Experimental details of these powder XRD measurements are given in Section S2.1. In (a) and (b), the peak with dominant intensity at $2\theta \approx 28°$ has been truncated. Differences in the relative peak intensities between (a), (b), and (c) are a consequence of preferred orientation.

The 3D-ED data were indexed and integrated using APEX4 software,[39] giving the following unit cell with monoclinic metric symmetry: a = 6.82(15) Å, b = 17.8(4) Å, c = 9.9(2) Å, β = 108.16(4)° (V = 1142 Å^3). Attempts to merge the 3D-ED data from different microcrystals did not prove satisfactory (see Section S2.2 for more details). Instead, the best data set (with a completeness of 84%) out of the 15 data sets collected was

https://doi.org/10.1021/acs.cgd.4c01717
Cryst. Growth Des. XXXX, XXX, XXX−XXX

used for the structure solution and refinement calculations described below. The most likely space groups were assigned as $P2_1/n$, $P2_1/a$, or $P2_1/c$, and structure solution was carried out independently in each case, as discussed below. The number (Z) of molecules of xanthine in the unit cell was established based on the reasonable assumption that xanthine should have a similar crystal density to a chemically similar molecule such as guanine (1.73 g cm^{-3} for the β polymorph of guanine[38]). On this basis, the number of molecules of xanthine in the unit cell may be deduced, from the known unit cell volume, to be Z = 8 (calculated crystal density, 1.74 g cm^{-3}). As the space groups under consideration have multiplicity 4, the number of crystallographically independent molecules of xanthine is Z' = 2 in each case. This information is required in setting up the structural models for the direct-space structure solution calculations. Independent evidence that the material studied is not a hydrate phase or solvate phase of xanthine was obtained from thermal analysis (see Section S2.3); in particular, TGA data show no mass loss on heating from ambient temperature to the temperature (ca. 350 °C) at which decomposition begins to occur.

Structure solution from the 3D-ED data was carried out using the direct-space genetic algorithm (GA) technique in the program EAGER, which was developed originally for structure solution from powder XRD data[40−46] and has now been extended for structure solution from 3D-ED data.[38,47−49] In setting up the direct-space structure solution calculations, the molecular model was obtained by carrying out DFT geometry optimization calculations (Section S4.1) for isolated molecules in the two tautomeric forms of xanthine shown in Figure 1. These tautomers (denoted here as A and B, but often named as N7H and N9H, respectively) have been assigned from previous computational studies[50−52] as the two tautomers of lowest energy. From DFT calculations using the Gaussian 09 program[53] (with basis set 6-311+G(2d,p) and the following three functionals: B3LYP, PBE and PBE0), the geometry optimized molecular structure of tautomer A is lower in energy than tautomer B by ca. 39 kJ mol^{-1} (the energy difference calculated using the three different functionals is in the range 38.9−39.7 kJ mol^{-1}; see Section S4.1). This result is in agreement with previous studies by Šponer et al.[50] and Raczyńska et al.,[52] which reported that tautomer A is lower in energy by 38.1 and 36.0 kJ mol^{-1}, respectively; another study[51] also concluded that tautomer A is lower in energy but by a smaller amount (17.5 kJ mol^{-1}).

In our direct-space GA structure-solution calculations from the 3D-ED data, the molecular model was taken as the geometry-optimized tautomer A from our DFT calculations, with two crystallographically independent molecules in the asymmetric unit. Each trial crystal structure was defined by 12 variables (three positional variables and three orientational variables for each molecule). For each space group ($P2_1/c$, $P2_1/n$, $P2_1/a$), 40 independent GA structure-solution calculations were carried out, in each case starting from a randomly generated initial population of 100 trial structures. In each GA calculation, the population was allowed to evolve for 200 generations, with 10 mating operations and 50 mutation operations per generation.

For space group $P2_1/a$, the best structure solution (with lowest R_F) from the GA calculations gave a significantly better fit to the 3D-ED data (R_F = 30.93%) than the best structure solutions for $P2_1/n$ (R_F = 40.58%) and $P2_1/c$ (R_F = 42.95%). Moreover, the structure giving the best fit to the 3D-ED data was obtained in 18 of the 40 independent GA calculations for $P2_1/a$. The best structure solution was considered to be structurally and chemically sensible (for example, all hydrogen-bond donor and acceptor groups in the xanthine molecules are engaged in geometrically reasonable hydrogen bonding) and was used as the initial model for structure refinement, which was carried out (as a kinematical refinement) from the 3D-ED data using SHELX.[54,55]

As unit cell parameters determined from powder XRD data are more reliable than those from 3D-ED data, the unit cell parameters for xanthine were also determined from powder XRD data. However, given the small number of peaks of significant intensity in the powder XRD data (Figure 2), the use of standard software for indexing powder XRD data proved unsuccessful. Instead, a "first-principles" approach (see Section S3.1) was applied for unit cell determination, based on assigning the Miller indices (hkl) of five peaks in a synchrotron powder XRD data set from knowledge of the indexing of the 3D-ED data, which allowed the following "initial unit cell" to be determined from the powder XRD data: a = 6.888(12) Å, b = 17.910(14) Å, c = 9.878(18) Å, β = 108.37(26)° (V = 1156.49(351) Å^3). After completing structure refinement from the 3D-ED data using this initial unit cell, a further determination of the unit cell was carried out by profile fitting of the powder XRD data (see Figure S4 and Section S3.1) using the Le Bail method; the initial unit cell from the first-principles approach was used as the starting point for the Le Bail fitting process, which gave the following "final unit cell": a = 6.8970(9) Å, b = 17.9258(27) Å, c = 9.8896(13) Å, β = 108.192(8)° (V = 1161.58(31) Å^3). We note that the esds in these unit cell parameters are significantly lower than those for the initial unit cell determined by the first-principles approach, and this final unit cell was used in our final structure refinement from the 3D-ED data, producing the crystal structure of xanthine (Figure 3) discussed below. As discussed in Section S3.2, a difference Fourier map calculated for the plane of the hydrogen-bonded sheet is consistent with the assignment of tautomer A as the major tautomer of xanthine present in the crystal structure.

Subjecting the final refined structure to periodic DFT-D geometry optimization (using the CASTEP program;[56,57] see Section S4.2) with fixed unit cell results in only minor atomic displacements (Figure 4), with a root-mean-squared deviation (RMSD) in atomic positions of 0.031 Å for non-H atoms and 0.044 Å for all atoms, confirming that the final structure determined from the 3D-ED data represents a minimum on the energy landscape.

Description of the Crystal Structure of Xanthine. In common with certain other purines (guanine,[38,58,59] hypoxanthine,[60,61] and adenine[62,63]), xanthine forms a layered crystal structure containing planar hydrogen-bonded sheets (Figure 3a). The sheets are parallel to the crystallographic $(10\bar{1})$ plane (which contains the unit cell vectors $\boldsymbol{b}$ and $\boldsymbol{a}$+$\boldsymbol{c}$). The mean deviation of the atom positions relative to the mean plane of the sheet in the refined structure is 0.076 Å (which decreases slightly to 0.066 Å following DFT-D geometry optimization). A given sheet contains the two crystallographically independent molecules (labeled 1 and 2 in Figure 3a), and the other molecules in the sheet are generated by the 2_1-screw operation. Adjacent sheets are related by the a-glide operation, with a perpendicular distance of 3.19 Å between adjacent sheets. The structural relationship between adjacent sheets (viewed perpendicular to the plane of the sheets in

https://doi.org/10.1021/acs.cgd.4c01717
Cryst. Growth Des. XXXX, XXX, XXX−XXX

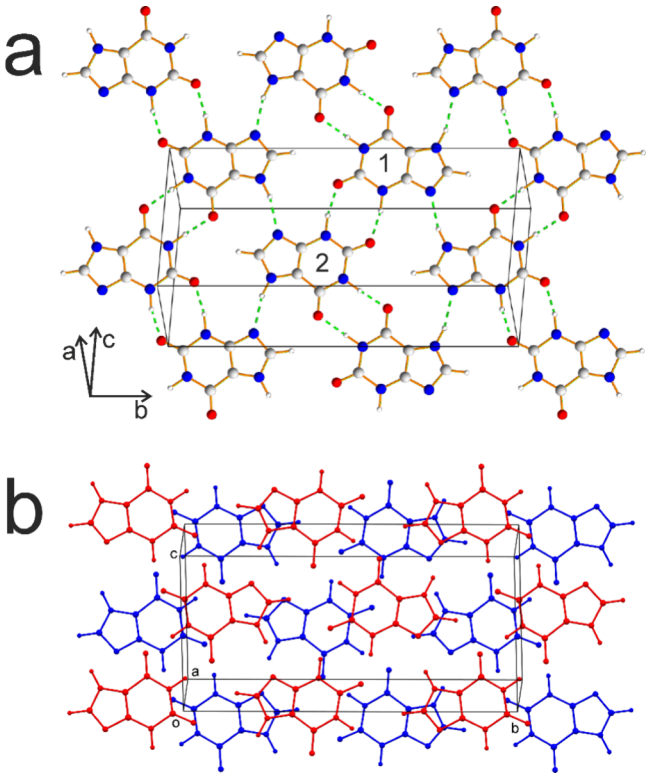

Figure 3. Crystal structure of xanthine (containing tautomer A) refined from 3D-ED data, showing (a) a single hydrogen-bonded sheet (hydrogen bonds are indicated by green dashed lines; the two crystallographically independent molecules are labeled 1 and 2), and (b) the structural relationship between adjacent sheets (shown in blue and red), which are related by the *a*-glide symmetry operation.

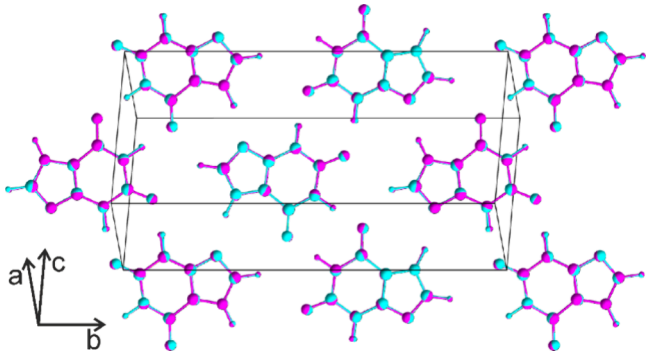

Figure 4. Overlay of the crystal structure of xanthine from the final structure refinement (cyan) and after subjecting the refined structure to periodic DFT-D geometry optimization with fixed unit cell (magenta).

Figure 3b) suggests that there are no significant $\pi\cdots\pi$ interactions between adjacent layers, although more detailed computational studies would be required to provide a more rigorous assessment of the nature of the intersheet interactions.

Within the hydrogen-bonded sheet, all hydrogen-bond donor and acceptor groups in the xanthine molecule are engaged in intermolecular hydrogen bonds, which may be categorized as (a) a cyclic hydrogen-bonded motif ($R_2^2(8)$ in graph set notation) comprising two N−H···O=C interactions between a molecule of type 1 and a molecule of type 2 (note that the center of the $R_2^2(8)$ ring is *not* a crystallographic inversion center), and (b) an N−H···N interaction between a molecule of type 1 and a molecule of type 2. Each molecule is involved in two interaction motifs of type (a), and zigzag chains of molecules linked by these interactions run along the [101] direction (parallel to ***a***+***c***). Each molecule is involved in two interactions of type (b) with different neighboring molecules (a given molecule acts as the N−H donor in one case and as the N acceptor in the other), and chains of molecules linked by these interactions also propagate along the [101] direction. From Figure 3a, it is clear that the set of local hydrogen-bonding interactions for the two crystallographically independent molecules (labeled 1 and 2) are very similar.

The crystal structure of xanthine bears some resemblance to the crystal structures of three other purines: adenine,[62,63] guanine,[38,58,59] and hypoxanthine.[60,61] For each of these other purines, two polymorphs are known, all of which are based on layered structures containing hydrogen-bonded sheets. As in the crystal structure of xanthine, the hydrogen-bonded sheets in the two polymorphs of guanine and in the triclinic polymorph[60] of hypoxanthine are essentially planar. In contrast, the hydrogen-bonded sheets in the monoclinic polymorph[61] of hypoxanthine and in the two polymorphs of adenine are significantly less planar and have a more undulating topology. For guanine, the hydrogen-bonding connectivity within the sheets is the same for the two polymorphs, which differ in the stacking of adjacent sheets, whereas for adenine, the hydrogen-bonding connectivity within the sheets differs significantly between the two polymorphs. For the two polymorphs of hypoxanthine, the hydrogen-bonding connectivity within the sheets is the same, even though the degree of planarity of the sheets differs for the two polymorphs, as noted above. Interestingly, the hydrogen-bonding connectivity in the two polymorphs of hypoxanthine shares several features in common with the structure of xanthine, albeit with fewer hydrogen bonds per molecule in the hypoxanthine crystal structures on account of the fact that one N−H group and one C=O group in the xanthine molecule are "replaced" by an N group and a C−H group, respectively, in hypoxanthine. Thus, the hydrogen-bonded sheets in the two polymorphs of hypoxanthine contain chains of molecules linked by N−H···N interactions of type (b), as in the structure of xanthine (see Figure 3a), and each hypoxanthine molecule forms a motif of type (a) with *one* neighboring molecule; in contrast, each molecule in the structure of xanthine forms motifs of type (a) with *two* neighboring molecules (see Figure 3a) as a result of the additional N−H and C=O groups per molecule.

Assessment of Tautomerism in the Crystal Structure. While our structure determination from the 3D-ED data was carried out using tautomer A, we note that the corresponding crystal structure containing tautomer B would be essentially identical, with the only significant difference being the position of one H atom per molecule (Figure 5). In particular, the crystal structure containing tautomer B would differ from the crystal structure of tautomer A only in terms of the H atom position in each intermolecular N−H···N hydrogen bond (i.e., N−H···N versus N···H−N) in the structure. To explore this issue further, we have assessed the relative energies of the crystal structures containing tautomer A and tautomer B based on periodic DFT-D geometry optimization calculations.

For tautomer A, the final refined crystal structure was used as the starting point for DFT-D geometry optimization. For tautomer B, the crystal structure was generated simply by shifting the H atom along each N−H···N hydrogen bond in

https://doi.org/10.1021/acs.cgd.4c01717
Cryst. Growth Des. XXXX, XXX, XXX−XXX

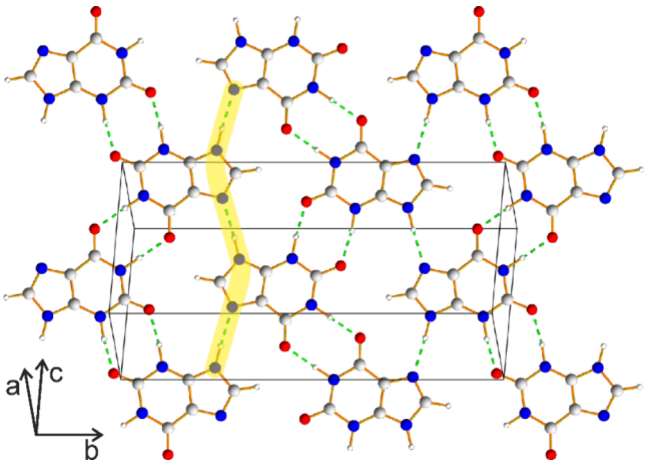

Figure 5. Crystal structure of xanthine containing tautomer B generated from DFT-D geometry optimization with fixed unit cell. From comparison to Figure 3a, the structures containing tautomers A and B are isostructural and differ only in the position of the H atoms within the chains of N−H···N hydrogen bonds that run along the [101] direction (one chain of this type is highlighted in yellow).

the crystal structure of tautomer A (following geometry optimization), which converts every molecule from tautomer A to tautomer B. The crystal structure of tautomer B generated in this way (which has the same unit cell and space group as the crystal structure of tautomer A) was subjected to periodic DFT-D geometry optimization with fixed unit cell. From these calculations, the geometry optimized crystal structure of tautomer A is lower in energy (by 5.60 kJ mol^{-1} per molecule) than the geometry optimized crystal structure of tautomer B. Interestingly, the optimized crystal structures for tautomers A and B are essentially identical (except for the H atom that differs in position for the two tautomers), with an RMSD in atomic positions between the two structures of only 0.078 Å for non-H atoms and 0.083 Å for all atoms (excluding the H atom that differs in position for tautomers A and B).

While tautomer A is lower in energy than tautomer B both for the isolated molecule (see above) and for the crystal structure, the difference in energy (per molecule of xanthine) between the two tautomeric crystal structures (5.60 kJ mol^{-1} per molecule) is significantly *lower* than the difference in energy between the isolated molecules of tautomers A and B (ca. 39 kJ mol^{-1} per molecule; see above), which suggests that the *intermolecular* contributions to the total energy of the crystal structure are more favorable for tautomer B than tautomer A, possibly as a result of the formation of stronger hydrogen-bonding in the crystal structure of tautomer B. A similar case in which a less-stable tautomer for the isolated molecule gives rise to a crystal structure with a more favorable intermolecular contribution to the total energy has been reported for alloxazine.[64]

As the crystal structures containing tautomers A and B of xanthine are isostructural (see Figures 3a and 5 and Figure S7) and as there is only a relatively small energy difference between them, it is plausible that the crystal structure of xanthine at ambient temperature may actually contain a population of tautomer B within the structure comprising predominantly tautomer A. Based on a simple Boltzmann calculation (see Section S5 for more details), the percentage of tautomer B that may be expected to exist in the structure at T = 298 K is estimated, from the equation $P_B(T) = 100/[1 + \exp(\Delta E/RT)]$ with ΔE = 5.60 kJ mol^{-1}, to be ca. 9.4%. While it may be challenging to establish the presence of a proportion of tautomer B at the level of around 10% or less in the structure refinement from 3D-ED data, various spectroscopic techniques (including solid-state NMR) may represent a more sensitive approach for investigating this issue.

CONCLUDING REMARKS

The solid-state structural properties of xanthine reported here serve to demonstrate the significant potential to exploit 3D-ED for structure determination of microcrystalline materials, especially in cases for which structure determination from single-crystal XRD and/or powder XRD is challenging. The present work also highlights the advantages of adopting a multitechnique approach for structure determination in such cases, with the process of structure determination from 3D-ED data enhanced by complementary information from periodic DFT-D calculations and powder XRD data.

To the best of our knowledge, polymorphism has not yet been reported for xanthine, although it would seem plausible for polymorphic structures to exist, for example based on different stacking arrangements of the type of hydrogen-bonded sheet observed in the crystal structure reported here. We note that, from our DSC study (see Section S2.3), there is no evidence that any phase transition (e.g., to form another polymorph) occurs on heating the sample of xanthine from ambient temperature to the temperature (ca. 350 °C) at which decomposition begins to occur.

As highlighted above, knowledge of the crystal structure is clearly essential in order to advance a deeper understanding of the role of crystalline xanthine in biological systems and processes. However, it is important to recall that the crystal structure reported here was determined for a synthetic sample of xanthine, and the structural properties of biogenic crystals of xanthine have not yet been reported.

Finally, another aspect of the solid-state structural properties of xanthine that merits future investigation is the possibility, suggested by the results of our DFT-D studies, that the crystal structure may contain a small population of tautomer B within a crystal structure comprising predominantly tautomer A. The application of a range of other techniques, including a variety of spectroscopic methods, may be expected to yield greater insights into this aspect in due course.

At a late stage of preparing this paper, we have become aware of a conference proceeding[65] and a preprint[66] discussing the crystal structure determination of xanthine. From the information given in these documents, the material studied is the same phase of xanthine reported in the present paper.

ASSOCIATED CONTENT

Data Availability Statement

Additional supporting experimental data for this article may be accessed at: 10.17035/cardiff.28053602.v1.

Supporting Information

The Supporting Information is available free of charge at https://pubs.acs.org/doi/10.1021/acs.cgd.4c01717.

Detailed materials and methods sections for: sample preparation and characterization, measurement and analysis of powder XRD data, measurement and analysis of 3D-ED data, thermal analysis (TGA and DSC), unit cell determination from powder XRD data, structure solution and refinement from 3D-ED data, DFT

https://doi.org/10.1021/acs.cgd.4c01717
Cryst. Growth Des. XXXX, XXX, XXX−XXX

calculations on the isolated xanthine molecule as tautomers A and B, periodic DFT-D calculations on the crystal structure of xanthine, and Boltzmann calculation to estimate the percentage of tautomer B in the crystal structure (PDF)

Accession Codes

Deposition Numbers 2403946 and 2410250 contain the supplementary crystallographic data for this paper. These data can be obtained free of charge via the joint Cambridge Crystallographic Data Centre (CCDC) and Fachinformationszentrum Karlsruhe Access Structures service.

AUTHOR INFORMATION

Corresponding Author

Kenneth D. M. Harris − *School of Chemistry, Cardiff University, Cardiff CF10 3AT Wales, U.K.;* orcid.org/0000-0001-7855-8598; Email: HarrisKDM@cardiff.ac.uk

Authors

Colan E. Hughes − *School of Chemistry, Cardiff University, Cardiff CF10 3AT Wales, U.K.;* orcid.org/0000-0003-2374-2763

Benson M. Kariuki − *School of Chemistry, Cardiff University, Cardiff CF10 3AT Wales, U.K.;* orcid.org/0000-0002-8658-3897

Abrar Almetahr − *School of Chemistry, Cardiff University, Cardiff CF10 3AT Wales, U.K.*

Jessica Saint-Mart − *School of Chemistry, Cardiff University, Cardiff CF10 3AT Wales, U.K.*

Andrew Williams − *School of Chemistry, Cardiff University, Cardiff CF10 3AT Wales, U.K.*

Laura Samperisi − *Eldico Scientific AG, Villigen, Aargau 5234, Switzerland*

Complete contact information is available at: https://pubs.acs.org/10.1021/acs.cgd.4c01717

Notes

The authors declare no competing financial interest.

ACKNOWLEDGMENTS

We are grateful to Cardiff University for support (to K.D.M.H., B.M.K., C.E.H., A.A.), to Advanced Research Computing at Cardiff (ARCCA) and Supercomputing Wales for computational resources, and to Jazan University, Saudi Arabia, for a Ph.D. studentship (to A.A.). Diamond Light Source is thanked for the award of beamtime on I11 (proposal no. EE19366). We thank Dr. Greg Shaw and Dr. James Hayward for assistance with TGA and DSC measurements.

REFERENCES

(1) Pais, V. M.; Lowe, G.; Lallas, C. D.; Preminger, G. M.; Assimos, D. G. Xanthine urolithiasis. *Urology* **2006**, *67*, 1084.e9−1084.e11.

(2) Wigner, P.; Gręboswski, R.; Bijak, M.; Szemraj, J.; Saluk-Bijak, J. The Molecular Aspect of Nephrolithiasis Development. *Cells* **2021**, *10*, 1926.

(3) White, R. N.; Tick, N. T.; White, H. L. Naturally occurring xanthine urolithiasis in a domestic shorthair cat. *J. Small Animal Practice* **1997**, *38*, 299−301.

(4) Tsuchida, S.; Kagi, A.; Koyama, H.; Tagawa, M. Xanthine urolithiasis in a cat: a case report and evaluation of a candidate gene for xanthine dehydrogenase. *J. Feline Medicine Surgery* **2007**, *9*, 503−508.

(5) Flegel, T.; Freistadt, R.; Haider, W. Xanthine urolithiasis in a dachshund. *Vet. Rec.* **1998**, *143*, 420−423.

(6) Sikora, P.; Pijanowska, M.; Majewski, M.; Bienias, B.; Borzecka, H.; Zajaczkowska, M. Acute renal failure due to bilateral xanthine urolithiasis in a boy with Lesch-Nyhan syndrome. *Pediatr. Nephrol.* **2006**, *21*, 1045−1047.

(7) Grases, F.; Costa-Bauza, A.; Roig, J.; Rodriguez, A. Xanthine urolithiasis: Inhibitors of xanthine crystallization. *PLoS One* **2018**, *13*, No. e0198881.

(8) Böhm, A.; Pass, G. The ocelli of Archaeognatha (Hexapoda): functional morphology, pigment migration and chemical nature of the reflective tapetum. *J. Exp. Biol.* **2016**, *219*, 3039−3048.

(9) Wagner, A.; Wen, Q.; Pinsk, N.; Palmer, B. A. Functional molecular crystals in biology. *Isr. J. Chem.* **2021**, *61*, 668−678.

(10) Friedman, O.; Böhm, A.; Rechav, K.; Pinkas, I.; Brumfeld, V.; Pass, G.; Weiner, S.; Addadi, L. Structural organization of xanthine crystals in the median ocellus of a member of the ancestral insect group Archaeognatha. *J. Struct. Biol.* **2022**, *214*, 107834.

(11) Hou, X.; Wang, Y.; Song, X.; Gao, J.; Ma, Y. Biomimetic synthesis of single-crystalline anhydrous xanthine nanoplates in an aqueous solution with high reflectivity. *Soft Matter* **2024**, *20*, 4422−4433.

(12) Niazov-Elkan, A.; Shepelenko, M.; Alus, L.; Kazes, M.; Houben, L.; Rechav, K.; Leitus, G.; Kossoy, A.; Feldman, Y.; Kronik, L.; Vekilov, P. G.; Oron, D. Surface-guided crystallization of xanthine derivatives for optical metamaterial applications. *Adv. Mater.* **2024**, *36*, 2306996.

(13) Pinsk, N.; Wagner, A.; Cohen, L.; Smalley, C. J. H.; Hughes, C. E.; Zhang, G.; Pavan, M. J.; Casati, N.; Jantschke, A.; Goobes, G.; Harris, K. D. M.; Palmer, B. A. Biogenic guanine crystals are organic alloys of guanine and other purine metabolites. *J. Am. Chem. Soc.* **2022**, *144*, 5180−5189.

(14) Wagner, A.; Hill, A.; Lemcoff, T.; Livne, E.; Avtalion, N.; Casati, N.; Kariuki, B. M.; Graber, E. R.; Harris, K. D. M.; Cruz-Cabeza, A. J.; Palmer, B. A. Rationalizing the influence of small-molecule dopants on guanine crystal morphology. *Chem. Mater.* **2024**, *36*, 8910−8919.

(15) Biradha, K.; Samai, S.; Maity, A. C.; Goswami, S. Supramolecular assembly of protonated xanthine alkaloids in their perchlorate salts. *Cryst. Growth Des.* **2010**, *10*, 937−942.

(16) Mizuno, H.; Fujiwara, T.; Tomita, K. The crystal and molecular structure of the sodium salt of xanthine. *Bull. Chem. Soc. Jpn.* **1969**, *42*, 3099−3105.

(17) Königsberger, E.; Wang, Z.; Seidel, J.; Wolf, G. Solubility and dissolution enthalpy of xanthine. *J. Chem. Thermodyn.* **2001**, *33*, 1−9.

(18) Klinenberg, J. R.; Goldfinger, S. E.; Seegmiller, J. E. The Effectiveness of the Xanthine Oxidase Inhibitor Allopurinol in the Treatment of Gout. *Ann. Int. Med.* **1965**, *62*, 639−647.

(19) Lister, J. H.; Caldbick, D. S. An Investigation into the Factors Governing the Aqueous Solubility of Xanthine (Purine-2,6-dione). *J. Appl. Chem. Biotechnol.* **1976**, *26*, 351−351.

(20) Saint-Mart, J. MChem Research Project. Cardiff University, 2018.

(21) Vincent, R.; Midgley, P. A. Double Conical Beam-Rocking System for Measurement of Integrated Electron-Diffraction Intensities. *Ultramicroscopy* **1994**, *53*, 271−282.

(22) Kolb, U.; Gorelik, T.; Kübel, C.; Otten, M. T.; Hubert, D. Towards automated diffraction tomography: Part I -: Data acquisition. *Ultramicroscopy* **2007**, *107*, 507−513.

(23) Zou, X.; Hovmöller, S. Electron crystallography: imaging and single-crystal diffraction from powders. *Acta Crystallogr., Sect. A: Found. Crystallogr.* **2008**, *64*, 149−160.

(24) Midgley, P. A.; Eggeman, A. S. Precession electron diffraction - a topical review. *IUCrJ.* **2015**, *2*, 126−136.

(25) Yun, Y. F.; Zou, X. D.; Hovmöller, S.; Wan, W. Three-dimensional electron diffraction as a complementary technique to powder X-ray diffraction for phase identification and structure solution of powders. *IUCrJ.* **2015**, *2*, 267−282.

(26) Palatinus, L.; Antunes Corrêa, C.; Steciuk, G.; Jacob, D.; Roussel, P.; Boullay, P.; Klementová, M.; Gemmi, M.; Kopeček, J.; Domeneghetti, M. C.; Cámara, F.; Petříček, V. Structure refinement using precession electron diffraction tomography and dynamical diffraction: tests on experimental data. *Acta Crystallogr., Sect. B: Struct. Sci. Cryst. Eng. Mater.* **2015**, *71*, 740−751.
(27) Palatinus, L.; Brázda, P.; Boullay, P.; Perez, O.; Klementová, M.; Petit, S.; Eigner, V.; Zaarour, M.; Mintova, S. Hydrogen positions in single nanocrystals revealed by electron diffraction. *Science* **2017**, *355*, 166−169.
(28) Gruene, T.; Wennmacher, J. T. C.; Zaubitzer, C.; Holstein, J. J.; Heidler, J.; Fecteau-Lefebvre, A.; De Carlo, S.; Müller, E.; Goldie, K. N.; Regeni, I.; Li, T.; Santiso-Quinones, G.; Steinfeld, G.; Handschin, S.; van Genderen, E.; van Bokhoven, J. A.; Clever, G. H.; Pantelic, R. Rapid Structure Determination of Microcrystalline Molecular Compounds Using Electron Diffraction. *Angew. Chem., Int. Ed.* **2018**, *57*, 16313−16317.
(29) Gemmi, M.; Mugnaioli, E.; Gorelik, T. E.; Kolb, U.; Palatinus, L.; Boullay, P.; Hovmöller, S.; Abrahams, J. P. 3D Electron Diffraction: The Nanocrystallography Revolution. *ACS Cent. Sci.* **2019**, *5*, 1315−1329.
(30) Brázda, P.; Palatinus, L.; Babor, M. Electron diffraction determines molecular absolute configuration in a pharmaceutical nanocrystal. *Science* **2019**, *364*, 667−669.
(31) Saha, A.; Nia, S. S.; Rodríguez, J. A. Electron Diffraction of 3D Molecular Crystals. *Chem. Rev.* **2022**, *122*, 13883−13914.
(32) Samperisi, L.; Zou, X.; Huang, Z. Three-dimensional electron diffraction: a powerful structural characterization technique for crystal engineering. *CrystEngComm* **2022**, *24*, 2719−2728.
(33) Woollam, G. R.; Das, P. P.; Mugnaioli, E.; Andrusenko, I.; Galanis, A. S.; van de Streek, J.; Nicolopoulos, S.; Gemmi, M.; Wagner, T. Structural analysis of metastable pharmaceutical loratadine form II, by 3D electron diffraction and DFT+D energy minimisation. *CrystEngComm* **2020**, *22*, 7490−7499.
(34) Lightowler, M.; Li, S. T.; Ou, X.; Zou, X. D.; Lu, M.; Xu, H. Y. Indomethacin Polymorph δ Revealed To Be Two Plastically Bendable Crystal Forms by 3D Electron Diffraction: Correcting a 47-Year-Old Misunderstanding. *Angew. Chem., Int. Ed.* **2022**, *61*, No. e202114985.
(35) Karothu, D. P.; Alhaddad, Z.; Göb, C. R.; Schürmann, C. J.; Bücker, R.; Naumov, P. The Elusive Structure of Levocetirizine Dihydrochloride Determined by Electron Diffraction. *Angew. Chem., Int. Ed.* **2023**, *62*, No. e202303761.
(36) Leung, H. W.; Copley, R. C. B.; Lampronti, G. I.; Day, S. J.; Saunders, L. K.; Johnstone, D. N.; Midgley, P. A. From formulation to structure: 3D electron diffraction for the structure solution of a new indomethacin polymorph from an amorphous solid dispersion. *IUCrJ.* **2024**, *11*, 744−748.
(37) Vinod, K.; Mathew, R.; Jandl, C.; Thomas, B.; Hariharan, M. Electron diffraction and solid-state NMR reveal the structure and exciton coupling in a eumelanin precursor. *Chem. Sci.* **2024**, *15*, 16015−16024.
(38) Wagner, A.; Merkelbach, J.; Samperisi, L.; Pinsk, N.; Kariuki, B. M.; Hughes, C. E.; Harris, K. D. M.; Palmer, B. A. Structure determination of biogenic crystals directly from 3D electron diffraction data. *Cryst. Growth Des.* **2024**, *24*, 899−905.
(39) *Apex Suite of Crystallographic Software, APEX4*; Bruker AXS Inc.: 2022.
(40) Kariuki, B. M.; Serrano-González, H.; Johnston, R. L.; Harris, K. D. M. The Application of a Genetic Algorithm for Solving Crystal Structures from Powder Diffraction Data. *Chem. Phys. Lett.* **1997**, *280*, 189−195.
(41) Kariuki, B. M.; Psallidas, K.; Harris, K. D. M.; Johnston, R. L.; Lancaster, R. W.; Staniforth, S. E.; Cooper, S. M. Structure determination of a steroid directly from powder diffraction data. *Chem. Commun.* **1999**, 1677−1678.
(42) Cheung, E. Y.; McCabe, E. E.; Harris, K. D. M.; Johnston, R. L.; Tedesco, E.; Raja, K. M. P.; Balaram, P. C-H···O Hydrogen bond mediated chain reversal in a peptide containing a γ-amino acid residue, determined directly from powder X-ray diffraction data. *Angew. Chem., Int. Ed.* **2002**, *41*, 494−496.
(43) Habershon, S.; Harris, K. D. M.; Johnston, R. L. Development of a multipopulation parallel genetic algorithm for structure solution from powder diffraction data. *J. Comput. Chem.* **2003**, *24*, 1766−1774.
(44) Guo, F.; Harris, K. D. M. Structural Understanding of a Molecular Material that is Accessed only by a Solid-state Desolvation Process: The scope of modern powder X-ray diffraction techniques. *J. Am. Chem. Soc.* **2005**, *127*, 7314−7315.
(45) Ma, X.; Lim, G. K.; Harris, K. D. M.; Apperley, D. C.; Horton, P. N.; Hursthouse, M. B.; James, S. L. Efficient, scalable, and solvent-free mechanochemical synthesis of the OLED material Alq_3 (q = 8-hydroxyquinolinate). *Cryst. Growth Des.* **2012**, *12*, 5869−5872.
(46) Williams, P. A.; Hughes, C. E.; Harris, K. D. M. L-Lysine: Exploiting Powder X-ray Diffraction to Complete the Set of Crystal Structures of the 20 Directly Encoded Proteinogenic Amino Acids. *Angew. Chem., Int. Ed.* **2015**, *54*, 3973−3977.
(47) Sun, T.; Hughes, C. E.; Guo, L.; Wei, L.; Harris, K. D. M.; Zhang, Y.; Ma, Y. Direct-space structure determination of covalent organic frameworks from 3D electron diffraction data. *Angew. Chem., Int. Ed.* **2020**, *59*, 22638−22644.
(48) Smalley, C. J. H.; Hoskyns, H. E.; Hughes, C. E.; Johnstone, D. N.; Willhammar, T.; Young, M. T.; Pickard, C. J.; Logsdail, A. J.; Midgley, P. A.; Harris, K. D. M. A structure determination protocol based on combined analysis of 3D-ED data, powder XRD data, solid-state NMR data and DFT-D calculations reveals the structure of a new polymorph of L-tyrosine. *Chem. Sci.* **2022**, *13*, 5277−5288.
(49) Smalley, C. J. H.; Hughes, C. E.; Hildebrand, M.; Aizen, R.; Bauer, M.; Yamano, A.; Levy, D.; Mirsky, S. K.; Shaked, N. T.; Young, M. T.; Kolb, U.; Gazit, E.; Kronik, L.; Harris, K. D. M. Understanding the Solid-State Structure of Riboflavin through a Multitechnique Approach. *Cryst. Growth Des.* **2024**, *24*, 6256−6266.
(50) Šponer, J.; Leszczyński, J. Tautomerism of Xanthine: The Second-Order Møller-Plesset Study. *Struct. Chem.* **1995**, *6*, 281−286.
(51) Kondratyuk, I. V.; Samijlenko, S. P.; Kolomiets', I. M.; Hovorun, D. M. Prototropic molecular-zwitterionic tautomerism of xanthine and hypoxanthine. *J. Mol. Struct.* **2000**, *523*, 109−118.
(52) Raczyńska, E. D.; Kamińska, B. Structural and thermochemical consequences of prototropy and ionization for the biomolecule xanthine in vacuo. *J. Chem. Thermodyn.* **2022**, *171*, 106788.
(53) Frisch, M. J.; Trucks, G. W.; Schlegel, H. B.; Scuseria, G. E.; Robb, M. A.; Cheeseman, J. R.; Scalmani, G.; Barone, V.; Mennucci, B.; Petersson, G. A.; Nakatsuji, H.; Caricato, M.; Li, X.; Hratchian, H. P.; Izmaylov, A. F.; Bloino, J.; Zheng, G.; Sonnenberg, J. L.; Hada, M.; Ehara, M.; Toyota, K.; Fukuda, R.; Hasegawa, J.; Ishida, M.; Nakajima, T.; Honda, Y.; Kitao, O.; Nakai, H.; Vreven, T.; Montgomery, J. A., Jr; Peralta, J. E.; Ogliaro, F.; Bearpark, M.; Heyd, J. J.; Brothers, E.; Kudin, K. N.; Staroverov, V. N.; Keith, T.; Kobayashi, R.; Normand, J.; Raghavachari, K.; Rendell, A.; Burant, J. C.; Iyengar, S. S.; Tomasi, J.; Cossi, M.; Rega, N.; Millam, J. M.; Klene, M.; Knox, J. E.; Cross, J. B.; Bakken, V.; Adamo, C.; Jaramillo, J.; Gomperts, R.; Stratmann, R. E.; Yazyev, O.; Austin, A. J.; Cammi, R.; Pomelli, C.; Ochterski, J. W.; Martin, R. L.; Morokuma, K.; Zakrzewski, V. G.; Voth, G. A.; Salvador, P.; Dannenberg, J. J.; Dapprich, S.; Daniels, A. D.; Farkas, Ö.; Foresman, J. B.; Ortiz, J. V.; Cioslowski, J.; Fox, D. J. *Gaussian 09, Revision D.01*; Gaussian, Inc.: 2013.
(54) Sheldrick, G. M. A Short History of SHELX. *Acta Crystallogr., Sect. A: Found. Crystallogr.* **2008**, *64*, 112−122.
(55) Sheldrick, G. M. SHELXT - Integrated Space-Group and Crystal-Structure Determination. *Acta Crystallogr., Sect. A: Found. Adv.* **2015**, *71*, 3−8.
(56) Clark, S. J.; Segall, M. D.; Pickard, C. J.; Hasnip, P. J.; Probert, M. J.; Refson, K.; Payne, M. C. First principles methods using CASTEP. *Z. Kristallogr.* **2005**, *220*, 567−570.
(57) Segall, M. D.; Lindan, P. J. D.; Probert, M. J.; Pickard, C. J.; Hasnip, P. J.; Clark, S. J.; Payne, M. C. First-principles simulation: ideas, illustrations and the CASTEP code. *J. Phys. Cond. Matt.* **2002**, *14*, 2717−2744.

https://doi.org/10.1021/acs.cgd.4c01717
Cryst. Growth Des. XXXX, XXX, XXX−XXX

(58) Guille, K.; Clegg, W. Anhydrous guanine: a synchrotron study. *Acta Crystallogr., Sect. C: Cryst. Struct. Commun.* **2006**, *62*, o515−o517.
(59) Hirsch, A.; Gur, D.; Polishchuk, I.; Levy, D.; Pokroy, B.; Cruz-Cabeza, A. J.; Addadi, L.; Kronik, L.; Leiserowitz, L. "Guanigma": The Revised Structure of Biogenic Anhydrous Guanine. *Chem. Mater.* **2015**, *27*, 8289−8297.
(60) Schmalle, H. W.; Hänggi, G.; Dubler, E. Structure of hypoxanthine. *Acta Crystallogr., Sect. C: Cryst. Struct. Commun.* **1988**, *44*, 732−736.
(61) Yang, R.-Q.; Xie, Y.-R. A monoclinic polymorph of hypoxanthine. *Acta Crystallogr., Sect. E: Struct. Rep.* **2007**, *63*, o3309.
(62) Mahapatra, S.; Nayak, S. K.; Prathapa, S. J.; Guru Row, T. N. Anhydrous Adenine: Crystallization, Structure, and Correlation with Other Nucleobases. *Cryst. Growth Des.* **2008**, *8*, 1223−1225.
(63) Stolar, T.; Lukin, S.; Požar, J.; Rubčić, M.; Day, G. M.; Biljan, I.; Jung, D. Š.; Horvat, G.; Užarević, K.; Meštrović, E.; Halasz, I. Solid-State Chemistry and Polymorphism of the Nucleobase Adenine. *Cryst. Growth Des.* **2016**, *16*, 3262−3270.
(64) Smalley, C. J. H.; Logsdail, A. J.; Hughes, C. E.; Iuga, D.; Young, M. T.; Harris, K. D. M. Solid-state structural properties of alloxazine determined from powder XRD data in conjunction with DFT-D calculations and solid-state NMR spectroscopy: unraveling the tautomeric identity and pathways for tautomeric interconversion. *Cryst. Growth Des.* **2022**, *22*, 524−534.
(65) Leung, H. W.; Copley, R. C. B.; Laulainen, J. E. M.; Johnstone, D. N.; Midgley, P. A. Combining Scanning Nanobeam Electron Diffraction with 3D Electron Diffraction to Investigate Crystal Defects. *Microsc. Microanal.* **2024**, *30*, 1820−1822.
(66) Leung, H. W.; Copley, R. C. B.; Lampronti, G. I.; Day, S. J.; Saunders, L. K.; Johnstone, D. N.; Midgley, P. A. Revealing the Crystal Structure of the Purine Base Xanthine with 3D Electron Diffraction. *ChemRxiv*, 2024. DOI: 10.26434/chemrxiv-2024-tlgvb.

https://doi.org/10.1021/acs.cgd.4c01717
Cryst. Growth Des. XXXX, XXX, XXX−XXX